Quantitative high dynamic range electron diffraction of polar nanodomains in Pb_2ScTaO_6

J. J. P. Peters[1], A. M. Sanchez[1], D. Walker[1], R. Whatmore[2], and R. Beanland[1]

[1]Department of Physics, University of Warwick, Coventry, CV4 7AL, United Kingdom

[2]Department of Materials, Royal School of Mines, South Kensington Campus, Imperial College London, London, SW7 2AZ, United Kingdom

Abstract

Highly B-site ordered Pb_2ScTaO_6 crystals have been studied as a function of temperature via dielectric spectroscopy and in-situ high dynamic range electron diffraction. The degree of ordering has been examined on the local and macroscopic scale and is determined to be 76 %. Novel analysis of the electron diffraction patterns provides structural information, with two types of antiferroelectric displacements determined to be present in the polar structure. It has then been found that a low temperature transition occurred on cooling at $\sim$ 210 K that is not present on heating. This phenomenon is discussed in terms of the freezing of dynamic polar nanodomains where a high density of domain walls creates a metastable state.

1 Introduction

Perovskite relaxor ferroelectrics have garnered interest due to their excellent dielectric, piezoelectric, electro-optic and pyroelectric properties[1–5] while exhibiting a range of phenomena that are still not fully understood.[6] The defining property of a relaxor is the frequency dependence of its dielectric permittivity, associated with the presence of small polarized regions that fluctuate at time-scales on the order of GHz.[7–11] Several theories have been put forward to explain this phenomenon, often invoking the presence of small random fields.[12–16]

Here, Pb_2ScTaO_6 (PST) is investigated, a double perovskite of form $A_2B'B''O_6$. This has the useful property of being ferroelectric when the Sc and Ta ions are fully ordered and a canonical relaxor when

they are disordered.[17–20] The ability to vary the level of ordering by choice of annealing parameters has made it one of the more widely studied relaxors.[8,21] Highly ordered PST has a unit cell doubled in all directions with respect to the prototype disordered (average structure $Pm\bar{3}m$) perovskite, with rock-salt ordering of the Sc and Ta cations giving a face-centred $Fm\bar{3}m$ structure with lattice parameter of 8.15 Å. Its paraelectric to ferroelectric phase transition at about 300 K, associated with a maximum in dielectric constant, is associated with a change in crystal structure from $Fm\bar{3}m$ to the rhombohedral $R3$ structure.[22,23] Below the $Fm\bar{3}m$ to $R3$ transition, highly ordered PST is switchable and able to maintain a permanent polarization, but it still possesses a large dielectric maximum in its unpoled state associated with rapidly-fluctuating polar nanodomains, sometimes named polar tweed.[24] Some studies of highly-ordered PST observed an incommensurate antiferroelectric phase in the range of 323-222 K.[25] In its disordered form, in common with many relaxors, disordered PST does not transform to a ferroelectric upon cooling while the polar nanoregions are expected to grow in size as the temperature decreases.[9,26] Whilst multiple studies have been conducted on formation of polar regions from the high temperature paraelectric phase,[24,27] there are relatively few studies at lower temperatures.

Here, the low temperature dynamics of highly ordered PST are examined using a combination of dielectric spectroscopy, X-ray diffraction (XRD) and transmission electron microscopy (TEM). Due to the dependence of functional properties on the level of ordering, a comprehensive analysis of the ordering has been conducted. High dynamic range (HDR) electron diffraction patterns are used to give a quantitative analysis of diffracted intensities and reveal a change of structure at ~ 210 K, attributed to the collapse of fluctuating polar tweed into a static ferroelectric.

2   Experimental details

PST ceramic samples were fabricated using the mixed oxide method described by Osbond and Whatmore.[28] Sc_2O_3 and Ta_2O_5 powders were milled together and then pre-reacted at 900 °C to form the wolframite phase $ScTaO_4$. This was reacted with PbO at 900 °C to form a single-phase perovskite powder, which was subsequently hot-pressed in Si_3N_4 tooling and an alumina grit packing medium at 40 MPa and 1200 °C for 6 hours.

Powder XRD was performed using a Bruker D5005 diffractometer with a Cu Kα source in the Bragg-Brentano geometry. Dielectric measurements were made on the same material as a function of temperature using a HP 4192A impedance analyser measuring AC resistance and capacitance with an AC voltage at 2.5, 10 and 40 kHz. Cooling was provided using liquid nitrogen with temperature control using an Oxford Instruments ITC503S. The entire system is kept under vacuum ($< 10^{-4}$ Torr) to avoid ice build up.
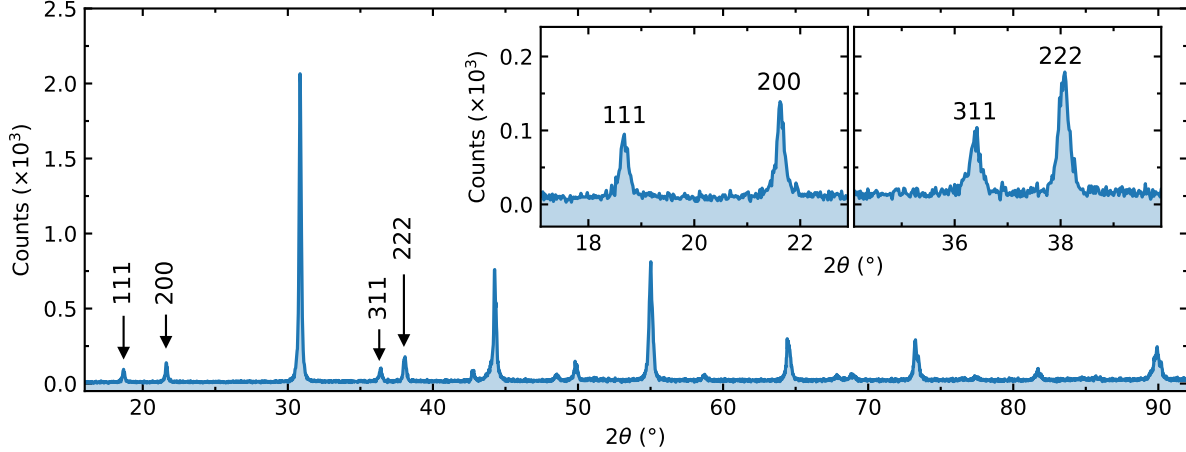
Figure 1: X-ray θ-2θ diffraction pattern from the bulk PST ceramic. Inset are close ups of the peaks used to determine the B-site ordering.

TEM samples were prepared by crushing the sample and mixing the ceramic with aluminium powder in a ration of ~1:10 PST:Al, followed by cold-rolling to form a ~50 μm thick solid sheet of Al with embedded PST crystals. Electron transparency was achieved using Ar^+ ion milling in a Gatan PIPS. In-situ low temperature studies were performed using a Gatan model 636 cooling holder and model 904 temperature controller. Maximum temperature ramping rates were 10 K s^{-1} with ~10 minutes allowed for the temperature to stabilize. Atomic resolution annular dark field (ADF) scanning transmission electron microscopy (STEM) images were recorded with a JEOL ARM200F over collection angles 45-180 mrad. High signal-to-noise images were formed by averaging multiple, rapidly acquired frames to remove scan distortions. All other TEM was performed on a JEOL 2100 with a LaB_6 source and a Gatan Orius CCD camera. For this camera saturation occurs at readout values of $\sim 1.4 \times 10^4$. HDR electron diffraction patterns were acquired by combining several images with varying exposures;[29] initial exposure times were 120 s with subsequent exposure times being halved until the CCD was no longer saturated, typically at a few ms. This simple HDR methodology extends the dynamic range of the CCD camera by a further 5 orders of magnitude to approximately 10^9, coping with high intensity electron signals whilst still detecting much weaker features. For a weak feature to be quantifiable, sufficient counting statistics are required, i.e. readout values between 10^2 and 10^3 for uncertainties of 10 % and 3 % respectively, with the result that quantification is possible with a precision of 10^{-8} of the incident beam intensity. More details of quantification procedures for HDR patterns are given later.
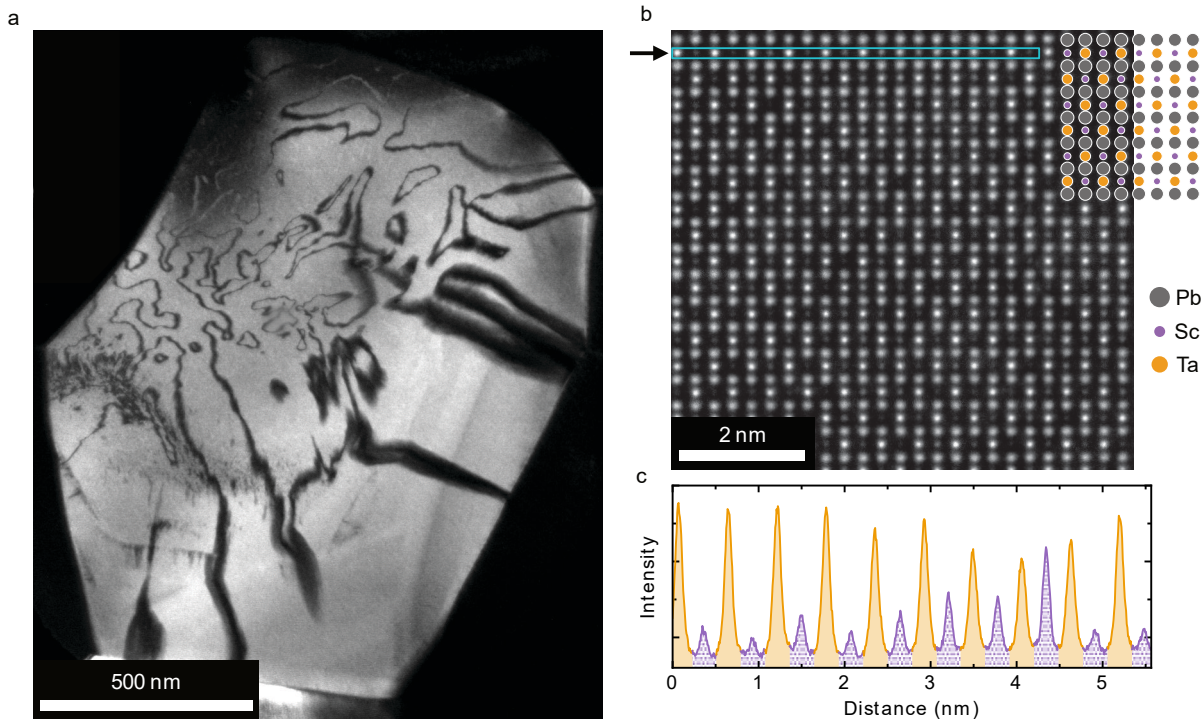
Figure 2: (a) Dark field $g = 111$ image of a single grain of PST. Bright and dark regions show ordered regions and APBs respectively. (b) Atomic resolution ADF image from (a) with strong ordering clearly evident. (c) An intensity line profile from the region indicated by an arrow in (b). Columns that are expected to contain Sc and Ta are highlighted purple (dotted shading) and orange (solid) respectively.

3 Results

3.1 B-cation ordering

As the functional properties of PST depend strongly on the degree of B-site cation ordering it is important to determine the degree of ordering for any specimen examined. Considering, for example, a Sc site, A, in the $Fm\bar{3}m$ unit cell, an ordering parameter may be defined as $S = O_{\mathrm{Sc}}(B_{\mathrm{Sc}}) - O_{\mathrm{Ta}}(B_{\mathrm{Sc}})$, where $O_X(B_{\mathrm{Sc}})$ is the average occupancy by atom X of the Sc sites, B_{Sc}, in the perfect structure. The ordering parameter S is zero for complete disorder and unity for perfect order. Any ordering of the B-cations can be detected by diffraction since it produces superlattice reflections that have all odd indices hkl which are nominally absent for the prototype disordered material (Note the pseudocubic $Fm\bar{3}m$ indexing is used throughout). Usefully, in partially ordered material the structure factor of these superlattice reflections is proportional to S. Conversely, reflections with all-even indices are insensitive to B-site ordering and can serve as a reference. While S may be expected to vary from place to place on a microscopic scale,[21] an average macroscopic value may be obtained from X-ray diffraction. Using diffraction vectors of similar magnitudes to minimise the effect of temperature factors, S can be estimated from the ratio of the 111 to 200 (or 311 to 222) intensities,

4

$$S^2 = \left(\frac{I_{111}}{I_{200}}\right)_{observed} \Big/ \left(\frac{I_{111}}{I_{200}}\right)_{perfect} \tag{1}$$

where I_{hkl} is the intensity of the hkl reflection and 'perfect' corresponds to perfectly ordered material.[30] The integrated intensities in a θ-2θ powder XRD pattern that would be obtained from perfectly ordered material, randomly oriented material may be calculated using tabulated atomic scattering factors.[31,32] Figure 1 shows a θ-2θ XRD pattern, which gives a macroscopic average value of $S = 0.76$ for the sample examined here. No crystallographic texture was observed.

The ordering has also been examined using electron microscopy, as shown in Fig. 2. Fig. 2(a) shows a dark field $g = 111$ electron micrograph, where highly ordered regions produce bright contrast and disordered anti-phase boundaries (APBs) appear as dark lines or bands. Attempting to quantify the ordering by considering the bright and dark regions as purely ordered and disordered, respectively, gives a value of $S = 0.85$. However, this calculation is naive as it relies on the assumption that the order is constant throughout the crystal thickness in the beam direction. In reality, APBs may be inclined with respect to the beam, small disordered regions may be embedded in an ordered matrix and even variations on a unit cell level will be present. Fig. 2(b) shows an atomic resolution ADF image at a $\langle 110 \rangle$ zone axis of a highly ordered region in Fig. 2(a). Here the TEM specimen is approximately 30 nm in thickness and the intensity of each column is determined by its average atomic number. In this projection there is no mixing between Sc and Ta columns in fully ordered material, with Sc columns ($Z = 21$) appearing faint compared to the brighter Ta ($Z = 73$) column. Ordering is evident in Fig. 2(b) although there is a noticeable variation in the intensities of the Sc and Ta columns, as shown in Fig. 2(c). This demonstrates that quite large variations in ordering occur at the nm scale, with some columns almost reaching equal intensity − as would be found in completely disordered material - while others approach 100 % ordering (see also supplementary Fig. S1). These data are consistent with the average value of $S = 0.76$ obtained by XRD.

3.2   Dielectric properties

The dielectric permittivity as a function of temperature during a cooling-heating cycle was measured with applied field frequencies of 2.5, 10 and 40 kHz, shown in Fig. 3. The prototypical transition maxima associated with the non-polar/polar phase transition can be seen at $T_m = 298$ K, whose lack of frequency dependence indicates that this highly-ordered PST is not a canonical relaxor. Approximately 20 K hysteresis is observed between the cooling and heating cycles. The polar state is usually found to be present on the low-temperature edge of this peak, i.e. at $T_c \approx 270$ K when cooling. In highly ordered material when the material is cooled without the application of an electric field, a 'polar tweed' phase has been proposed to
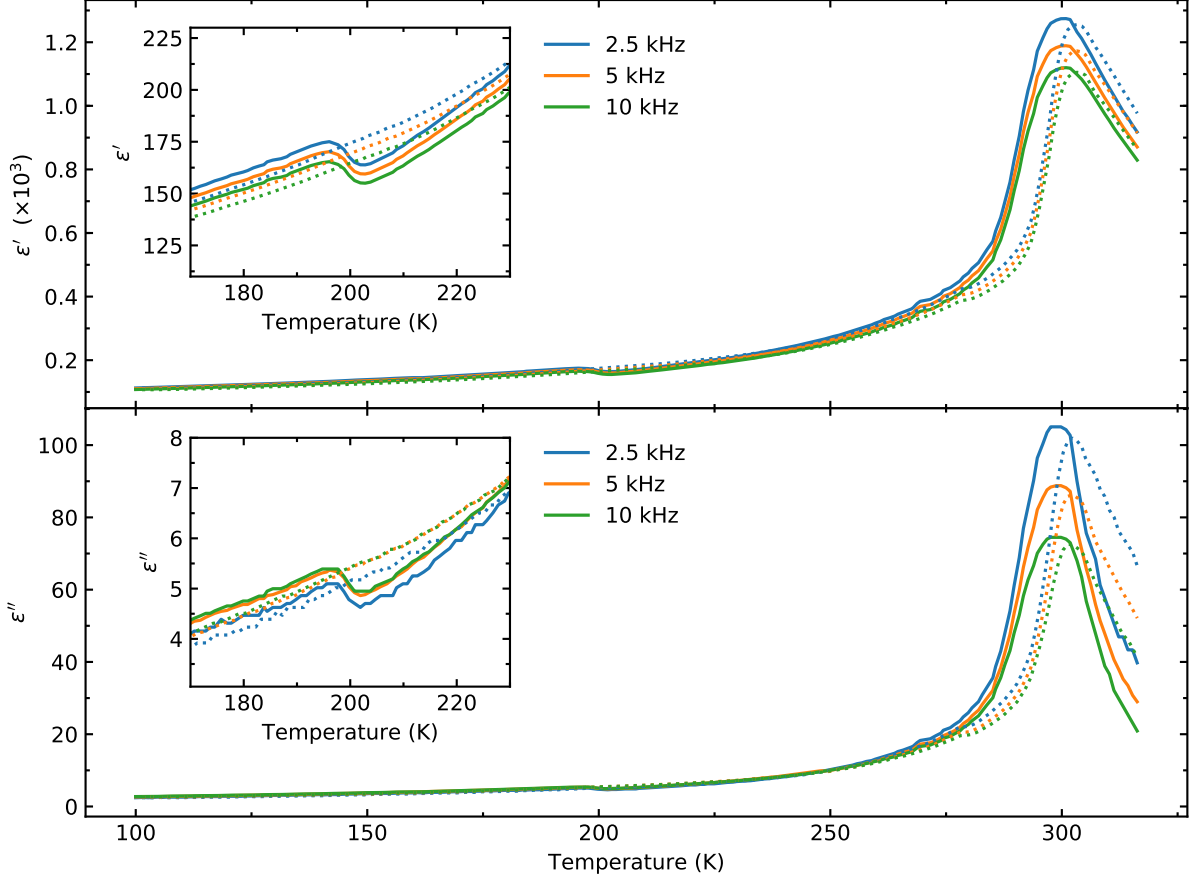
Figure 3: Real (top) and imaginary (bottom) parts of the dielectric permittivity as a function of temperature and for multiple frequencies of the applied field. Inset are magnified regions of the same data showing a peak starting at 205 K. Solid lines show cooling and dotted lines show heating.

form.[24, 27]

In TEM, domain structure is observed using dark field $g = 226$ imaging conditions at 270 K (supplementary Fig. S2). These domains are elongated along $\langle 110 \rangle$ directions and often show fluctuating contrast, consistent with polar domain reorientations.[33] There is some resemblance to the polar tweed microstructure[34, 35] and there appears to be little or no relationship between this domain structure and anti-phase boundaries, in agreement with previous observations.[21]

At lower temperatures, an additional inflection is also visible in the cooling curve at ~ 200 K. This may indicate a first-order transition from the polar tweed state to a conventional ferroelectric on cooling, as seen in previous studies. It has been proposed previously that the rhombohedral structure transitions to monoclinic below similar temperatures, though the possibility of domain wall pinning was also discussed.[36, 37] Here, this anomaly is not observed in the subsequent heating cycle, indicating that the high-temperature state may be metastable. In dark field TEM imaging, large domains were observed at ~ 200 K, suggesting that the
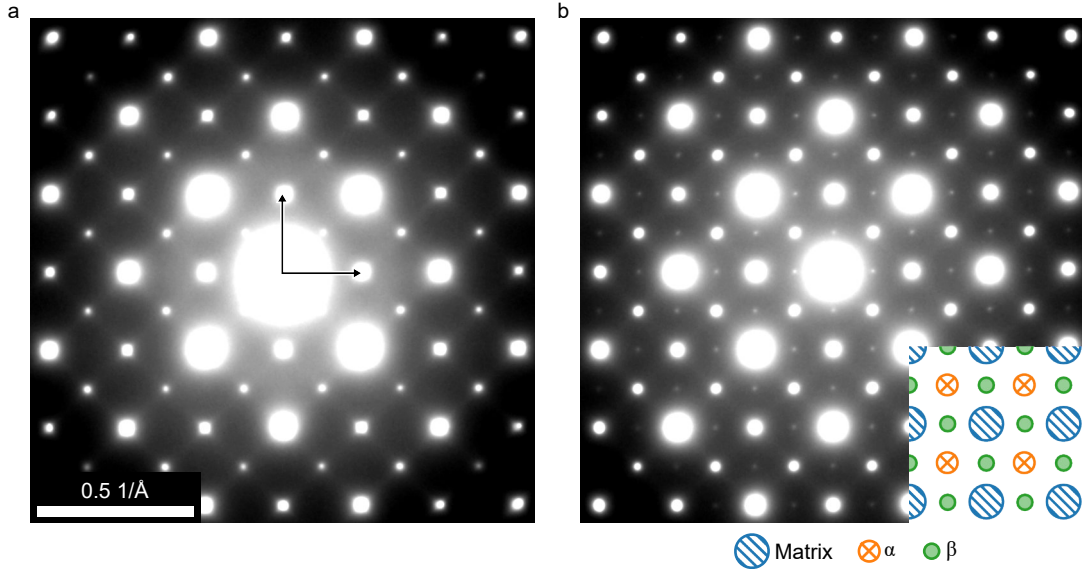
Figure 4: Room temperature (295 K), (a), and Cold (110 K), (b), $\langle 100 \rangle$ HDR diffraction patterns showing the additional α and β spots. Arrows on (a) show the 200, 020 basis for the matrix spots. Note that the image intensity scale follows a power law to show all the peaks at the same time.

transition is associated with the collapse of dynamic polar tweed to a static ferroelectric state. Nevertheless, some small regions still exhibited contrast fluctuations, though this may be associated with the electron beam. Heating associated with the electron beam is expected to be below 1 K for the conditions used for imaging and significantly less during acquisition of SAED patterns.[38] Nevertheless, manipulation of domain walls with a concentrated electron beam was possible (supplementary Fig. S3), likely due to localised charging of the sample.[21, 39]

3.3 HDR electron diffraction

In electron diffraction, B-site rock-salt ordering gives additional reflections in patterns taken along zone axes perpendicular to any direction with all-odd indices. In patterns where this is not the case, such as [001], ordering changes the intensity of a subset of the matrix spots but does not produce additional ones. Below T_c a set of weak additional spots appears, with integer indices of the form *odd odd 0* (e.g. 110) in the [001] pattern, known as α-spots.[21] At even lower temperatures another set of spots appears with indices *odd even 0* and *even odd 0* (e.g. 210), known as β-spots (Fig. 4). These spots indicate the formation of a polar structure with symmetry lower than the prototype $Fm\bar{3}m$ structure, in which reflections with mixed odd- and even-indices would be forbidden. These additional sets of spots are visible in $\langle 100 \rangle$ HDR selected area electron diffraction (SAED) patterns, as shown in Fig. 4 for temperatures of 295 K and 110 K. The use of HDR diffraction patterns allows a quantitative analysis of both the α- and β-spots, even though they are

weak (see supplementary information Fig. S4).

Since quantitative analysis of HDR diffracted electron intensities has not been performed before, some issues that arise must be addressed before going further. In quantitative X-ray diffraction it is usual to normalise all diffracted intensities with respect to the strongest diffracted beam, which itself is given an intensity of 100 %. This procedure allows quantification in cases where, for example, the crystal is smaller than the size of the X-ray beam and the directly transmitted beam cannot be used as a reference. However, such a procedure is not appropriate for electron diffraction, where dynamical diffraction effects redistribute intensity between reflections and even small ($< 0.1°$) changes in crystal orientation can have dramatic effects on strong diffracted beam intensities, making them an unreliable reference. This problem also affects the directly transmitted beam. Fortunately, the use of a selected area aperture means that all the signal has come from the crystal (though the same area must be used each time) and the captured electron diffraction pattern collects almost all of the scattered electrons. Thus the total intensity in the whole pattern is used as a reference, with the reasonable assumption that dynamical effects may redistribute intensity between strong beams, but the total captured intensity will be unaffected and give a good measure of the incident beam intensity, I_0. Some of the scattered intensity appears as diffuse background scattering between the diffracted beams (see Fig. S4(a)). For the weak reflections of interest, this background can be significantly more intense than the spots so is measured and removed using an annular region of appropriate size (supplementary Fig. S4(b) and (c)). Finally, a different problem arises in the measurement of the many spots that make up a family, such as the α-spots, which have different intensities due to different structure factors and increasing deviation from the Bragg condition away from the direct beam. Here, the mean of all intensities is used for each family with g-vector magnitudes less than or equal to the square defined by the 800-type spots. Using this procedure, accurate quantifiable integrated intensities as weak as $10^{-7} I_0$ are obtained.

Figure 5 shows the mean integrated intensities for α- and β-spots (I_α and I_β respectively) as a function of temperature for both cooling and heating cycles. Figure 5(a) shows that the profile for the α-spots increase as a square root law, $I_\alpha \propto (T_c - T)^{\frac{1}{2}}$. The behavior of the β-spots is more complex; at room temperature, the spots are not present in the HDR diffraction patterns and, on cooling, this remains the case until 220 K when a sharp increase in the signal is observed. From 210 K to 110 K, the β-spot intensity increases linearly, $I_\beta \propto (T_c - T)$, to an intensity of $\sim 2 \times 10^{-6}\ I_0$, roughly two orders of magnitude weaker than the α-spots. On reheating a continuous, linear decrease is observed with no discontinuity until $I_\beta \sim 0$ at $T = T_c$. This behavior matches the dielectric measurements in Fig. 3, where small temperature differences may be reconciled by the experimental setup (i.e. inefficient cooling through the TEM grid and sample holder).
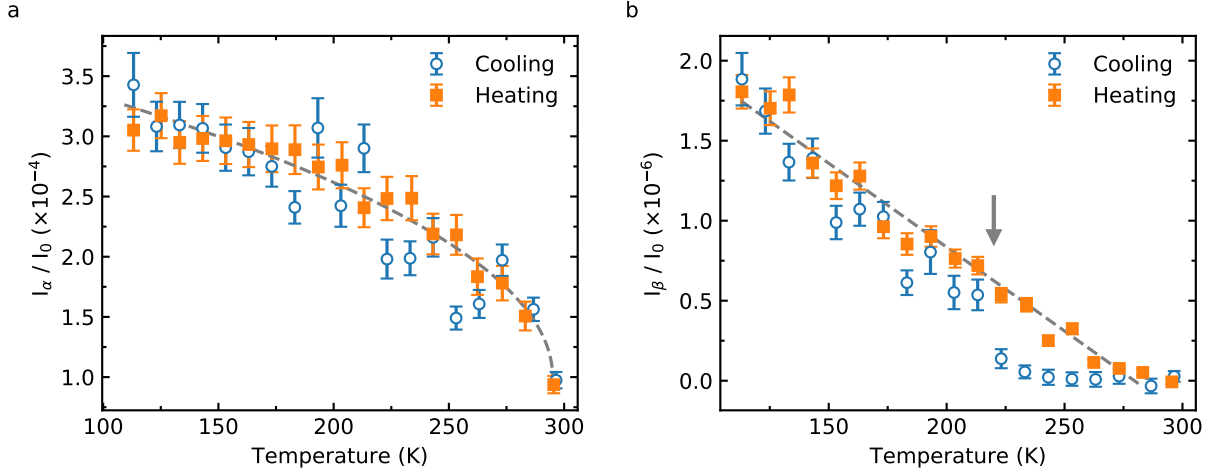
Figure 5: (a) Mean α-spot intensities for cooling (blue circles) and heating (orange squares) with a parabolic fit. (b) Mean β-spot intensities with an abrupt appearance upon cooling at ~ 210 K (arrowed). Error bars give the standard error of the mean.

3.4 Structural model

Starting from the ideal $Fm\bar{3}m$ structure (with no aditional spots in [001] electron diffraction patterns), the atoms are perturbed to form the additional spots. By confining the structure to the accepted $R3$ structure proposed by previous studies[23, 24, 40] and discounting movement that cannot produce extra spots (i.e. the shift of an entire cation sublattice will produce no extra spots), a structural model for the displacements can be built. The corresponding diffraction patterns can then be calculated using the kinematical theory of electron diffraction since the superstructure spots are weak. Here Kirkland's scattering factors[32] and Debye-Waller factors interpolated from Woodward and Baba-Kishi[40] have been used.

Two displacement schemes that were found to create α- and β-spots are shown in Fig. 6 along with their calculated intensities. It is found that α-spots are formed by correlated displacements of cations along the polar [111] axis but with neighbouring [111] columns displaced in the opposite direction (i.e. atoms on the 3-fold axis are displaced one way and atoms off the 3-fold axis are displaced oppositely). This forms a columnar antiferroelectric as shown in Fig. 6(a). On the other hand, β-spots are caused by the anti-correlated displacements of a rock-salt type antiferroelectric where all nearest neighbours have opposite displacements along [111] (Fig. 6(b)).

Unfortunately, while the form of displacements from the $Fm\bar{3}m$ sites is clear, it is not possible to *a-priori* distinguish between spots formed by A-cations and those formed by B-cations. I_α calculated for correlated Pb and Ta/Sc displacements is shown in Figure 6(c). An I_α comparable to those observed ($\sim 3 \times 10^{-4} I_0$) can be produced either by Pb displacements of 12 pm or Ta/Sc displacements of 32 pm (the Pb displacement

9
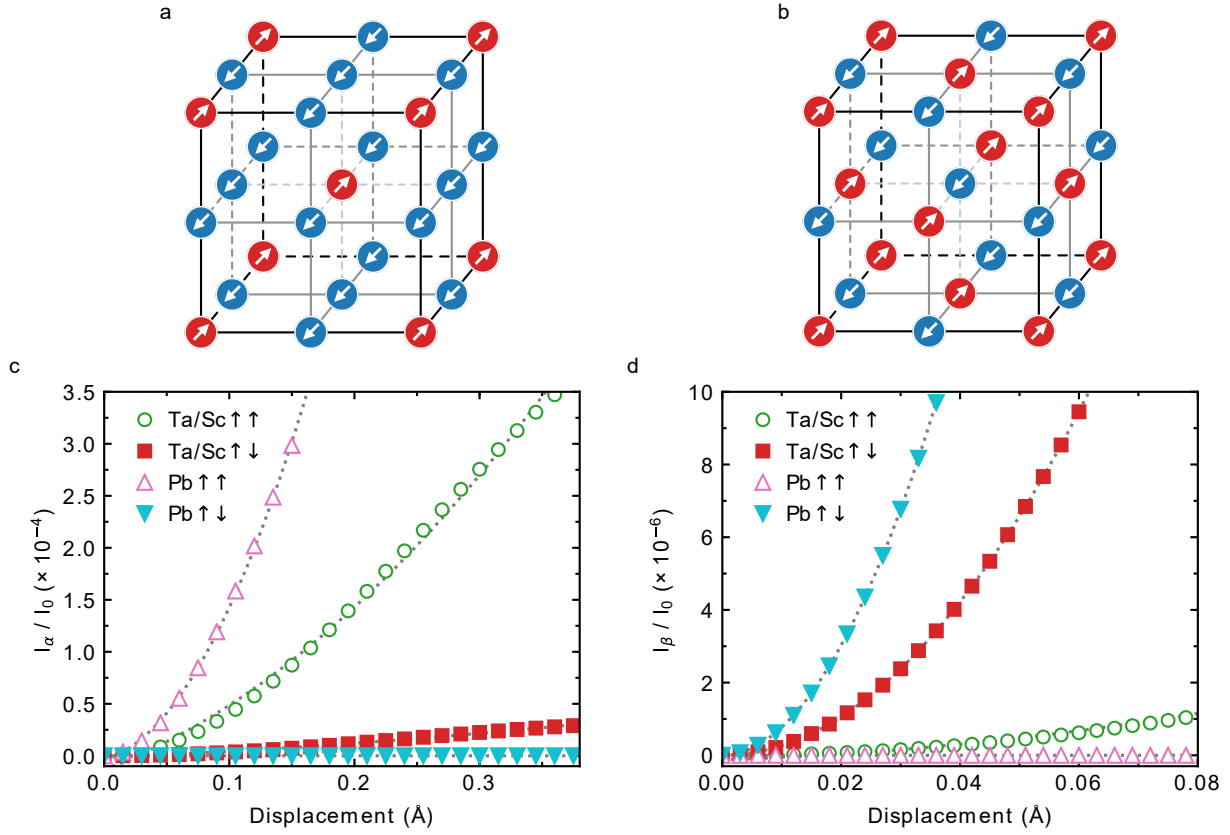
Figure 6: (a) Correlated [111] columnar (↑↑) displacement scheme. (b) Anti-correlated [111] (↑↓) displacement scheme. Arrows and colors indicate displacements along the [111] direction. (c) and (d) show mean α- and β-spot intensities as a function of displacements for both Ta/Sc and Pb ions. ↑↑ and ↑↓ correspond respectively to correlated and anti-correlated displacements for neighbors in the [111] direction.

is smaller simply because Pb scatters electrons more strongly than Ta/Sc). In both cases, I_α increases in proportion with the square of the displacement. Also shown on Fig. 6(c) are mean diffracted α-spot intensities produced by β-spot type displacements; it is apparent that observed α-spot intensities would require infeasibly large displacements. As an additional confirmation of this model, the correlated movements produce systematic α-spot absences along one $\langle 110 \rangle$ direction, agreeing with experimentally observed weaker α-spots along both $\langle 110 \rangle$ directions, presumably due to the presence of different orientational variants of the structure (supplementary Fig. S5).

Mean calculated β-spot intensities are shown in Fig. 6(d), again for both models and Pb and Ta/Sc displacements. Interestingly, β-spots can be produced by large α-type displacements of the Ta/Sc atoms. The different temperature behaviors of I_α and I_β imply that α-spots are formed by coupled displacements of Pb, consistent with previous studies.[21, 40, 41] Therefore, it may be expected that the β-spots are formed by ~ 3 pm antiferroelectric displacements of the Ta and Sc ions in a rock-salt pattern, which is pleasingly consistent with their rock-salt ordering pattern. The mean intensity I_β also increases in proportion with the square of the displacement; the smallest intensity measured, $\sim 10^{-7} I_0$ just below Tc, corresponds to a displacement of only 0.1 pm.

4   Discussion

The low-temperature structure has been determined by Woodward and Baba-Kishi[40] to be $R3$ using X-ray and neutron diffraction at 4 K, although difficulties were experienced due to broadening of superstructure spots leading them to fix the coordinates of the Sc and Ta ions and constrain O coordinates; the only unconstrained displacements were of a subset of the Pb atoms. Cooperative oxygen octahedral tilting was not detected. A mixture of correlated and anti-correlated displacements for crystallographically distinct cations is required to produce both α- and β-spots, and this behavior is indeed found in their model. Recently, a ferrielectric model has been proposed to explain the behavior of PST,[41] although only antiferroelectric Ta/Sc displacements were proposed, rather than the two antiferroelectric distortions seen in this work (it is not possible to measure potential ferroelectric displacements here). High energy electrons, with a much smaller wavelength than X-rays or neutrons and the ability to sample smaller volumes, have some advantages for analysis of these materials. excessive broadening of the superstructure spots are not observed here, presumably because Scherrer broadening is much smaller for electron diffraction and the material is uniform over the small region sampled. The nm-scale domain sizes close to T_c in combination with Scherrer broadening make the very weak reflections used for the analysis too diffuse to be seen in XRD or neutron diffraction. This means that the pm-scale correlated or anti-correlated atomic displacements are then only visible as

anomalously large thermal vibration parameters.[40, 42] Here, the domain structure is tracked to within a few degrees of T_c, although broadening effects become limiting eventually even for electron diffraction and fleeting correlations present in dynamic polar nanodomains above T_c are not detected.

4.1 Phase behavior

Several investigators have proposed a low temperature phase transition in PST. Baba-Kishi et al.[25] an incommensurate antiferroelectric phase between T_c and 223 K in highly ordered PST, though the associated satellite peaks are not observed in the electron diffraction patterns show here. Dawber et al.[36] proposed a rhombohedral to monoclinic phase transition at 233 K in ordered PST, although domain wall pinning was also considered a possibility. Abdulvakhidov et al.[37] also found various anomalies in PST at similar temperatures. Other studies of relaxors under an applied electric field have also found a transition from nanodomains to a long-range ferroelectric domain state with peaks in dielectric permittivity similar to Fig. 3.[12, 43] The metastability found here, combined with the dark field observation of the domains would suggest that this transition is associated with the domain pinning as the fluctuating nanodomains freeze into a static state. The high density of mobile domain walls in the fluctuating polar state may act to stabilise the fluctuating polarity due to low local domain-wall energies,[44] While Pb vacancies have been shown to inhibit the static ferroelectric state and may contribute to the metastability, the uniform Pb column intensities in Fig. 2(b) indicate such vacancies are not abundant here.[18] On reheating, the relatively low number of domain walls act as nucleation points for the continuous 'melting' of the ferroelectric state to dynamic polar nanodomains. This ties into previous analogies of relaxors to water/ice, made due to their similar dielectric properties,[44–46] where freezing melting asymmetries, similar to those observed here, can be found.[47, 48]

The presence of two distinct antiferroelectric distortions makes PST ferrielectric, rather than ferroelectric, and probably accounts for much of the relaxor behavior observed in material with different degrees of ordering. The quantitative nature of HDR electron diffraction, and the known points in k-space associated with the α and β-spots, allows a straightforward link to be made between the measured intensities and the associated ferroic order parameters. First, the order parameters Q_α and Q_β are defined as proportional to the respective displacements of cations that result in the α- and β spots. Then, using the square root relationship between the intensities and the displacements it is evident that $Q_\alpha \propto (T_c - T)^{\frac{1}{4}}$, showing tricritical behavior,[24] while $Q_\beta \propto (T_c - T)^{\frac{1}{2}}$ and indicates a second order phase transition.[49] Some coupling between these order parameters may be expected and the observation that T_c is common to both indicates this is at least bilinear. Q_β may be expected to correlate with the degree of B-site ordering, S, and the variety of behaviors seen in PST may be dictated by the changes in strength and coupling between Qα and Qβ leading to, for example,

the incommensurate antiferroelectric structures.[25]

5   Conclusions

Novel electron diffraction techniques have been employed to extract new information on the structure and dynamics of the polar fluctuations in highly ordered PST ceramic. This has allowed the exploration a little studied low temperature phase transition at 210 K that is associated with the transition from a dynamic polar system to a static one. The transition shows an asymmetry on heating and cooling that suggests a metastable state and indicates the importance of local domain wall energies. Supported by a comprehensive study of the ordering in the examined crystals, the work presented here adds yet another piece to the complex jigsaw puzzle in the understanding of relaxors and related materials. Furthermore, the novel analysis employed here expands the use of electron diffraction for quantitatively examining structural phenomena on the picometre scale.

Acknowledgements

References

[1] Kutnjak, Z., Petzelt, J. & Blinc, R. The giant electromechanical response in ferroelectric relaxors as a critical phenomenon. *Nature* **441**, 956–959 (2006).

[2] Shvartsman, V. V. & Lupascu, D. C. Lead-Free Relaxor Ferroelectrics. *Journal of the American Ceramic Society* **95**, 1–26 (2012).

[3] Bokov, A. A. & Ye, Z.-G. Recent progress in relaxor ferroelectrics with perovskite structure. *Journal of Materials Science* **41**, 31–52 (2006).

[4] Park, S.-E. & Shrout, T. R. Ultrahigh strain and piezoelectric behavior in relaxor based ferroelectric single crystals. *Journal of Applied Physics* **82**, 1804–1811 (1997).

[5] Qu, B., Du, H. & Yang, Z. Lead-free relaxor ferroelectric ceramics with high optical transparency and energy storage ability. *J. Mater. Chem. C* **4**, 1795–1803 (2016).

[6] Hehlen, B., Al-Sabbagh, M., Al-Zein, A. & Hlinka, J. Relaxor Ferroelectrics: Back to the Single-Soft-Mode Picture. *Physical Review Letters* **117** (2016).

[7] Burns, G. Crystalline ferroelectrics with glassy polarization behavior. *Physical Review B* **28**, 2527–2530 (1983).

[8] Setter, N. & Cross, L. E. The role of B-site cation disorder in diffuse phase transition behavior of perovskite ferroelectrics. *Journal of Applied Physics* **51**, 4356–4360 (1980).

[9] Cross, L. E. Relaxor ferroelectrics. *Ferroelectrics* **76**, 241–267 (1987).

[10] Bokov, A. A. & Ye, Z.-G. Dielectric Relaxation In Relaxor Ferroelectrics. *Journal of Advanced Dielectrics* **02**, 1241010 (2012).

[11] Blinc, R. *et al.* ^{207}Pb NMR study of the relaxor behavior in PbMg$_{1/3}$Nb$_{2/3}$O$_3$. *Physical Review B* **63** (2000).

[12] Westphal, V., Kleemann, W. & Glinchuk, M. D. Diffuse phase transitions and random-field-induced domain states of the "relaxor" ferroelectric PbMg$_{1/3}$Nb$_{2/3}$O$_3$. *Physical review letters* **68**, 847 (1992).

[13] Glinchuk, M. D. & Farhi, R. A random field theory based model for ferroelectric relaxors. *Journal of Physics: Condensed Matter* **8**, 6985 (1996).

[14] Fisch, R. Random-field models for relaxor ferroelectric behavior. *Physical Review B* **67** (2003).

[15] Kleemann, W. Random Fields In Relaxor Ferroelectrics — A Jubilee Review. *Journal of Advanced Dielectrics* **02**, 1241001 (2012).

[16] Pirc, R. Spherical random-bond–random-field model of relaxor ferroelectrics. *Physical Review B* **60**, 13470–13478 (1999).

[17] Stenger, C. G. F., Scholten, F. L. & Burggraaf, A. J. Ordering and diffuse phase transitions in Pb(Sc$_{0.5}$Ta$_{0.5}$)O$_3$ ceramics. *Solid State Communications* **32**, 989–992 (1979).

[18] Chu, F., Setter, N. & Tagantsev, A. K. The spontaneous relaxor-ferroelectric transition of Pb(Sc$_{0.5}$Ta$_{0.5}$)O$_3$. *Journal of Applied Physics* **74**, 5129–5134 (1993).

[19] Stenger, C. G. F. & Burggraaf, A. J. Order–disorder reactions in the ferroelectric perovskites Pb(Sc$_{1/2}$Nb$_{1/2}$)O$_3$ and Pb(Sc$_{1/2}$Ta$_{1/2}$)O$_3$. I. Kinetics of the ordering process. *physica status solidi (a)* **61**, 275–285 (1980).

[20] Stenger, C. G. F. & Burggraaf, A. J. Order–disorder reactions in the ferroelectric perovskites Pb(Sc$_{1/2}$Nb$_{1/2}$)O$_3$ and Pb(Sc$_{1/2}$Ta$_{1/2}$)O$_3$. II. Relation between ordering and properties. *physica status solidi (a)* **61**, 653–664 (1980).

[21] Randall, C. A., Barber, D. J., Whatmore, R. W. & Groves, P. A TEM study of ordering in the perovskite, Pb(Sc$_{1/2}$Ta$_{1/2}$)O$_3$. *Journal of Materials Science* **21**, 4456–4462 (1986).

[22] Sivasubramanian, V. Brillouin scattering studies of acoustic phonon modes and central peak in single-crystal Pb(Sc$_{1/2}$Ta$_{1/2}$)O$_3$. *Physical Review B* **85** (2012).

[23] Baba-Kishi, K. Z., Woodward, P. M. & Knight, K. The crystal structures of Pb$_2$ScTaO$_6$ and Pb$_2$ScNbO$_6$ in the paraelectric and ferroelectric states. *Ferroelectrics* **261**, 21–26 (2001).

[24] Aktas, O. *et al.* Ferroelectric precursor behavior in PbSc$_{0.5}$Ta$_{0.5}$O$_3$ detected by field-induced resonant piezoelectric spectroscopy. *Physical Review B* **88**, 174112 (2013).

[25] Baba-Kishi, K. Z. & Pasciak, M. An electron diffraction and Monte Carlo simulation study of an incommensurate antiferroelectric state in the relaxor ferroelectric Pb$_2$ScTaO$_6$. *Journal of Applied Crystallography* **43**, 140–150 (2010).

[26] Xu, G., Gehring, P. M. & Shirane, G. Coexistence and competition of local- and long-range polar orders in a ferroelectric relaxor. *Physical Review B* **74** (2006).

[27] Dul'kin, E., Salje, E. K. H., Aktas, O., Whatmore, R. W. & Roth, M. Ferroelectric precursor behavior of highly cation-ordered PbSc0.5ta0.5o3 detected by acoustic emission: Tweed and polar nanoregions. *Applied Physics Letters* **105**, 212901 (2014).

[28] Osbond, P. C. & Whatmore, R. W. DiC17: High dielectric constant ceramics in the PbSc$_{0.5}$Ta$_{0.5}$O$_3$-PbZrO$_3$ system. *Ferroelectrics* **133**, 159–161 (1992).

[29] Evans, K. & Beanland, R. High Dynamic Range Electron Imaging: The New Standard. *Microscopy and Microanalysis* **20**, 1601–1604 (2014).

[30] Setter, N. & Cross, L. E. The contribution of structural disorder to diffuse phase transitions in ferroelectrics. *Journal of Materials Science* **15**, 2478–2482 (1980).

[31] Doyle, P. A. & Turner, P. S. Relativistic Hartree–Fock X-ray and electron scattering factors. *Acta Crystallographica Section A: Crystal Physics, Diffraction, Theoretical and General Crystallography* **24**, 390–397 (1968).

[32] Kirkland, E. J. *Advanced Computing in Electron Microscopy* (Springer, New York, 2010), 2nd edn.

[33] Bursill, L. A., JuLin, P., Hua, Q. & Setter, N. Relationship between nanostructure and dielectric response of lead scandium tantalate — (I) structure and domain textures. *Physica B: Condensed Matter* **205**, 305–326 (1995).

[34] Salje, E. K. H., Hayward, S. A. & Lee, W. T. Ferroelastic phase transitions: structure and microstructure. *Acta Crystallographica Section A Foundations of Crystallography* **61**, 3–18 (2005).

[35] Salje, E. K. H. *et al.* Direct observation of polar tweed in LaAlO3. *Scientific Reports* **6**, 27193 (2016).

[36] Dawber, M., Ríos, S., Scott, J. F., Zhang, Q. & Whatmore, R. W. Cryogenic electrical studies of manganese-doped lead scandium tantalate thin films: Phase transitions or domain wall dynamics? *AIP Conference Proceedings* **582**, 1–10 (2001).

[37] Abdulvakhidov, K. G., Mardasova, I. V., Myasnikova, T. P., Vitchenko, M. A. & Oshaeva, E. N. Phase transitions in $PbSc_{0.5}Ta_{0.5}O_3$. *Technical Physics* **55**, 514–516 (2010).

[38] Egerton, R., Li, P. & Malac, M. Radiation damage in the TEM and SEM. *Micron* **35**, 399–409 (2004).

[39] Hart, J. L. *et al.* Electron-beam-induced ferroelectric domain behavior in the transmission electron microscope: Toward deterministic domain patterning. *Physical Review B* **94** (2016).

[40] Woodward, P. M. & Baba-Kishi, K. Z. Crystal structures of the relaxor oxide $Pb_2(ScTa)O_6$ in the paraelectric and ferroelectric states. *Journal of Applied Crystallography* **35**, 233–242 (2002).

[41] Mihailova, B., Maier, B., Steilmann, T., Dul'kin, E. & Roth, M. Electric-field-induced local structural phenomena in Pb-based ABO_3-type relaxor ferroelectrics. *IEEE Transactions on Ultrasonics, Ferroelectrics, and Frequency Control* **62**, 7–17 (2015).

[42] Maier, B. J. *Phase transitions in advanced relaxor-ferroelectric materials with a perovskite-type structure.* Ph.D. thesis, Universität Hamburg (2010).

[43] Arndt, H., Sauerbier, F., Schmidt, G. & Shebanov, L. A. Field-induced phase transition in $Pb(Mg_{1/3}Nb_{2/3})O_3$ single crystals. *Ferroelectrics* **79**, 145–148 (1988).

[44] Takenaka, H., Grinberg, I., Liu, S. & Rappe, A. M. Slush-like polar structures in single-crystal relaxors. *Nature* **546**, 391–395 (2017).

[45] Takenaka, H., Grinberg, I. & Rappe, A. M. Anisotropic Local Correlations and Dynamics in a Relaxor Ferroelectric. *Physical Review Letters* **110** (2013).

[46] Elton, D. C. & Fernández-Serra, M.-V. Polar nanoregions in water: A study of the dielectric properties of TIP4p/2005, TIP4p/2005f and TTM3f. *The Journal of Chemical Physics* **140**, 124504 (2014).

[47] Denoyel, R. & Pellenq, R. J. M. Simple Phenomenological Models for Phase Transitions in a Confined Geometry. 1: Melting and Solidification in a Cylindrical Pore. *Langmuir* **18**, 2710–2716 (2002).

[48] Petrov, O. & Furó, I. A study of freezing–melting hysteresis of water in different porous materials. Part I: Porous silica glasses. *Microporous and Mesoporous Materials* **138**, 221–227 (2011).

[49] Salje, E. K. H. *Phase transitions in ferroelastic and co-elastic crystals* (Cambridge University Press, Cambridge, England, 1990).

Supplementary material for Quantitative high dynamic range electron diffraction of polar nanodomains in Pb_2ScTaO_6

J. J. P. Peters[1], A. M. Sanchez[1], D. Walker[1], R. Whatmore[2], and R. Beanland[1]

[1]Department of Physics, University of Warwick, Coventry, CV4 7AL, United Kingdom

[2]Department of Materials, Royal School of Mines, South Kensington Campus, Imperial College London, London, SW7 2AZ, United Kingdom

1   Ordering

In annular dark field (ADF) scanning transmission electron microscope (STEM) images, the image intensity is approximately proportional to the square of the atomic number, Z^2, of the column the beam is incident to.[1] This relationship is useful for probing the composition of a structure such as the ordering in Pb_2ScTaO_6. Viewing the double perovskite structure along the 110 direction, the B-sites will align so as each column only contains one individual element (Ta or Sc) in the perfectly ordered structure. By examining the intensities of the columns, the level of mixing can be gauged. Figure S1 shows the intensity distributions of the Sc and Ta sites in a highly ordered region, showing a wide range of intensities for both columns with a small overlap. Intensities are calculated as the total intensity inside the Voronoi cell defined by the A- and B-sites.[2] This shows that the highly ordered regions still contain a degree of disorder that needs to be considered in any analysis.
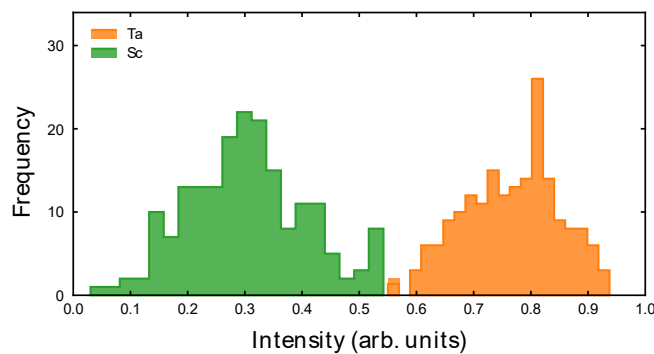

Figure S1: Histogram of the integrated intensities of the Sc (dark) and Ta (bright) columns from Fig. 2(b).
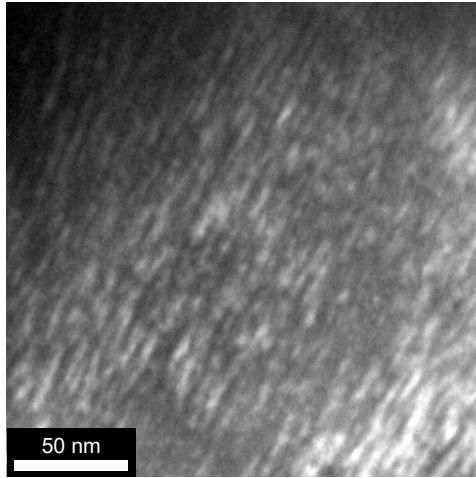
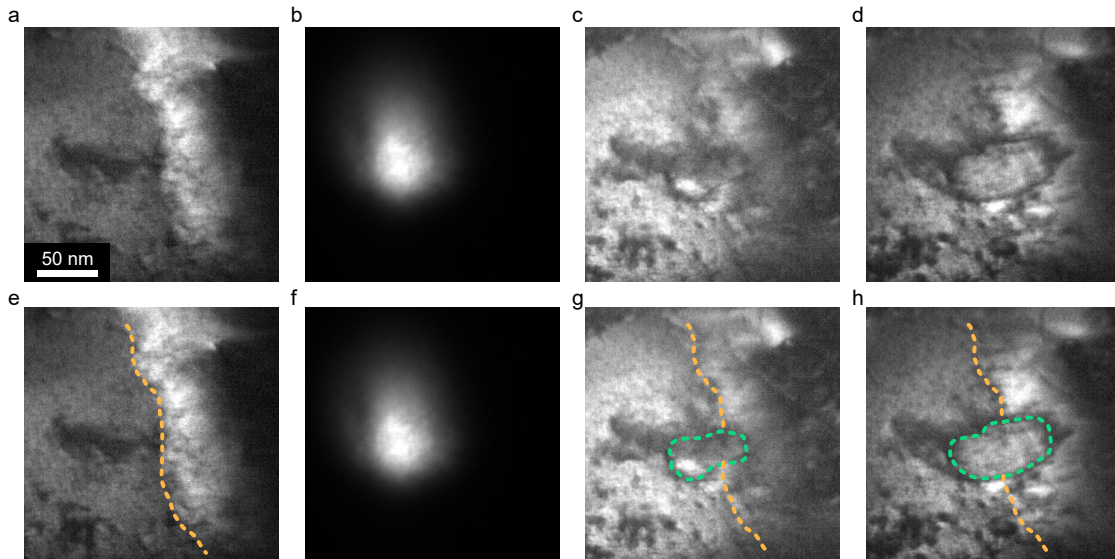Figure S2: Dark field TEM image showing the polar tweed structure as stripes from bottom-left to top right.

Figure S3: (a)-(d) time evolution of ferroelectric domains manipulated using the electron beam. (e)-(h) The same images as in (a)-(d) but with the domain walls highlighted. Images were recorded at 200 K.

2 Domain imaging

Using dark fild imaging by isolating one of the weak diffraction spots (for example 226), it is possible to image the polar nanodomains. Figure 2 shows such an image where the domain structure (or tweed) is clearly present as streaks from bottom left to top right. Such domain structure is present throughout our samples.

In dark field imaging it is possible to image the polar tweed and ferroelectric domains as shown in Fig. S2, where stripes can be seen. In contrast to the polar nano domains, Fig. S3 shows equivalent imaging at 200 K where the large ferroelectric domains can be seen as well as the ability to manipulate the domains simple by condensing the beam.
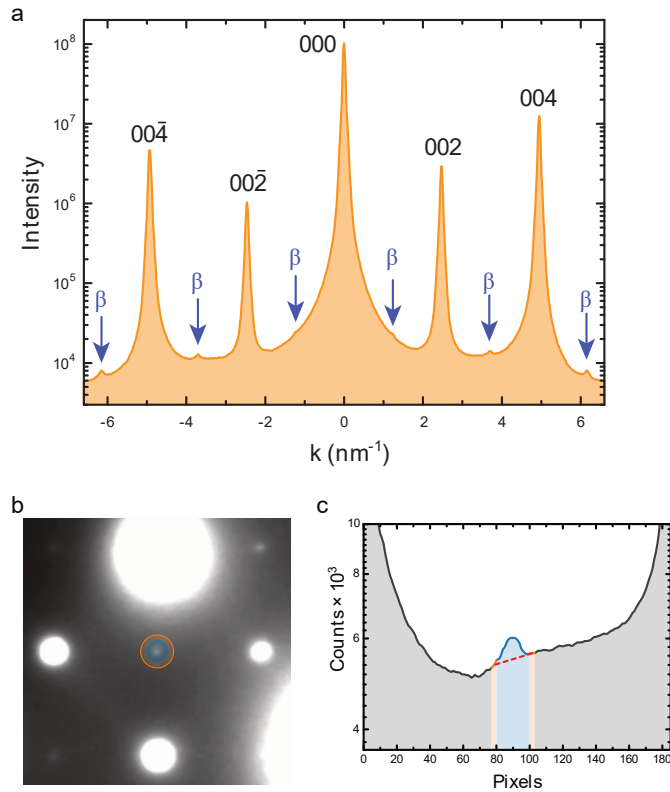
Figure S4: (a) Profile taken from Fig. 5(b) along the 200 direction. The β-spots have been labelled to highlight the difference in intensities. (b) and (c) demonstrate how the peak intensities were extracted. Orange shows the background region, blue the signal and the dashed red line demonstrates the interpolated background.

3 Diffraction intensity calculation

The intensity extraction for the experimental images is demonstrated in Fig. S4(b) and Fig. S4(c) for a weak β-spot. Two circles are defined, the signal (blue) and the background (orange). The average background is calculated within the ring, and then used to calculate the expected background signal within the signal area. This is subtracted from the total intensity within the signal region to give the peak intensity. To be able to compare data across several days or with different beam conditions, the intensity is divided by the total intensity in the diffraction patter (i.e. the total beam intensity for low enough campera lengths). Note that this method has the effect of assuming a linear change in background across the signal region (red line in Fig. S4(c)) and results in more accurate intensity measurements for smaller peaks. Therefore, this method is not practical for the larger matrix spots, where there is significant overlap of the peaks. However, the small β-spots are easily extracted even if they impinge on the shoulder of a larger peak (as seen in Fig. S1(a)).
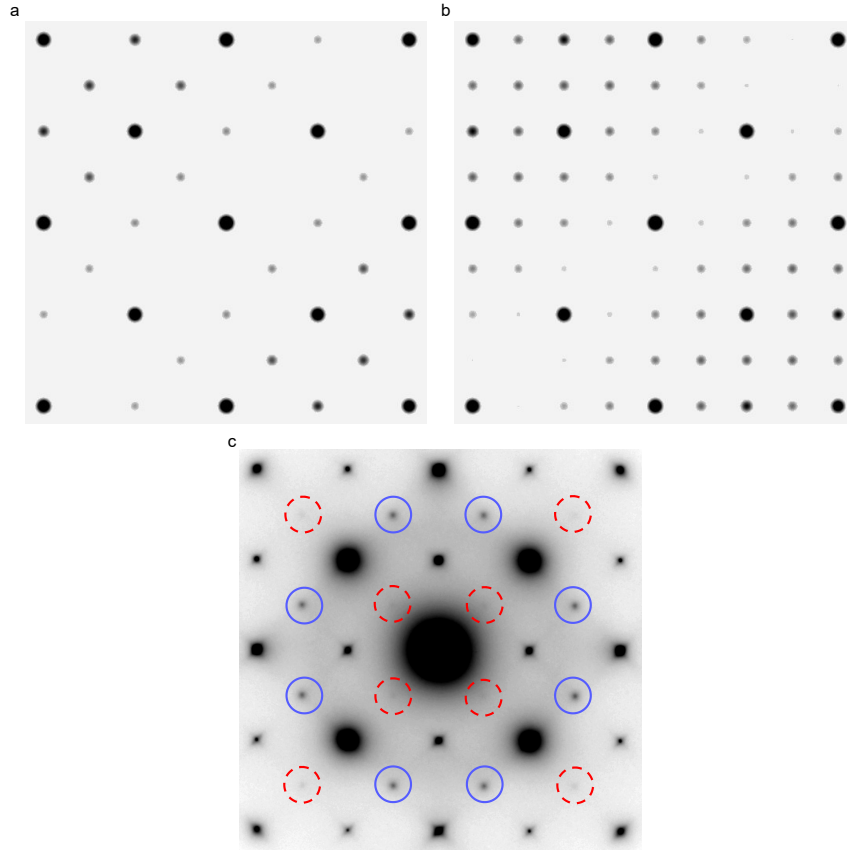
Figure S5: Calculated diffraction pattern from correlated, (a), and anticorrelated, (b), displacements for Pb atoms along the [111] direction. Systematic absences can be seen in the 110 direction (bottom-left to top-right). (c) Experimental image showing weakened α-spots in the 110 and $\bar{1}10$ directions (red dashed circles) compared to the other α-spots (blue solid circles). Contrast has been inverted for all images.

4 Systematic absences

The systematic absences in the diffraction patterns are shown in Fig. S5. It is clearly visible in the calculated images that there are missing α-spots along one of the 110 directions. Although these absences are not present in the experimental images, the spots are weakened (Fig. S5(c)). This is due to the thickness of the sample containing multiple orientations of the same structure, and the absences are a mixture of 110 and $\bar{1}10$ type.

References

[1] Bals, S., Kilaas, R. & Kisielowski, C. Nonlinear imaging using annular dark field TEM. *Ultramicroscopy* **104**, 281–289 (2005).

[2] Mostaed, A. *et al.* Atomic structure study of the pyrochlore $Yb_2Ti_2O_7$ and its relationship with low-temperature magnetic order. *Physical Review B* **95** (2017).